

# Improved O<sub>2</sub> evolution from a water splitting reaction over Er<sup>3+</sup> and Y<sup>3+</sup> co-doped tetragonal BiVO<sub>4</sub>

Cite this: *Catal. Sci. Technol.*, 2014, 4, 2042

S. Obregón and G. Colón\*

Received 14th January 2014,  
Accepted 28th February 2014

DOI: 10.1039/c4cy00050a

www.rsc.org/catalysis

Erbium–yttrium co-doped BiVO<sub>4</sub> with a tetragonal structure is synthesized by means of a surfactant free hydrothermal method. The studied photocatalyst shows good photoactivity under sun-like excitation for the degradation of methylene blue (MB) and for O<sub>2</sub> evolution. From structural and morphological characterization, it has been stated that the presence of lanthanides induces the stabilization of the tetragonal phase. This is probably due to the substitutional occupation that occurs in the BiVO<sub>4</sub> lattice. The photocatalytic performance under visible–NIR radiation clearly evidences the occurrence of an up-conversion process involved in the overall photo-electronic mechanism. The tetragonal phase Er<sub>0.0075</sub>Y<sub>0.03</sub>–Bi<sub>0.9625</sub>VO<sub>4</sub> system gives the highest O<sub>2</sub> evolution rate (425 μmol g<sup>−1</sup> h<sup>−1</sup>) under sun-like excitation, being 8 times higher than that attained for m-BiVO<sub>4</sub> (53 μmol g<sup>−1</sup> h<sup>−1</sup>).

## 1. Introduction

Nowadays, the recent socioeconomic demands concerning energy and environmental pollution have led to the progress of new green technologies such as photocatalysis.<sup>1,2</sup> Within this frame, in the last few years those working on heterogeneous photocatalysis have focused their attention toward the development of novel alternative materials to traditional TiO<sub>2</sub>, which are capable of using sunlight as a green energy source.<sup>3,4</sup> Since the discovery of photocatalytic water cleavage, plenty of effort has been put into developing new photocatalysts for overall water splitting, and some excellent results have been obtained.<sup>5,6</sup> Nevertheless, the efficiencies achieved are still far from those required for practical applications. A typical approach to accomplishing overall water splitting is to design a two coupled photoreaction called a Z-scheme system.<sup>7,8</sup> While H<sub>2</sub> production from aqueous solution containing sacrificial reagents has been demonstrated to be quite an efficient process, the O<sub>2</sub> production semi-reaction still remains a challenging redox process.<sup>9</sup> Hence, the synthesis of a highly active photocatalyst for the O<sub>2</sub> evolution reaction is quite important for enhancing the efficiency of solar-hydrogen conversion. In this sense, it has been stated that BiVO<sub>4</sub> is one of the most active systems for this reaction.<sup>10,11</sup> This is due to its relatively low band gap (2.4 eV for monoclinic BiVO<sub>4</sub>) and the adequate position of valence and conduction bands as compared to the redox potential for

water oxidation. As is widely known, the photocatalytic properties of BiVO<sub>4</sub> are strongly dependent on its morphology and microstructure.<sup>12–14</sup> Among the three main crystalline phases described (monoclinic scheelite, tetragonal zircon, and tetragonal scheelite), the monoclinic phase (m-BiVO<sub>4</sub>) appears as the only one which shows a high photoactivity for the O<sub>2</sub> evolution reaction under visible-light irradiation.<sup>15–17</sup> This is due to the particular structure of the valence band (which is formed by Bi 6s orbitals or a hybrid orbital of Bi 6s and O 2p) and the conduction band (formed by a V 3d orbital). This band configuration is responsible for its narrow band gap (*ca.* 2.4 eV) compared to 3.0 eV exhibited by the tetragonal phase.

A novel challenging approach, which would use solar light as efficiently as possible, consists of the assembly of a photocatalyst with a luminescent material.<sup>18–21</sup> Within this configuration we have recently described the assembly of TiO<sub>2</sub> with Er<sup>3+</sup> acting as the up-converting doping cation.<sup>22</sup> From those results, we proposed that the presence of Er<sup>3+</sup> doped into TiO<sub>2</sub> as a host matrix favors a double mechanism, under UV and vis-NIR excitation. We have also stated that Er<sup>3+</sup>-doping on BiVO<sub>4</sub> clearly stabilizes the tetragonal structure.<sup>23</sup> In this sense, a tentative cooperative mechanism has been proposed. Tetragonal phase stabilization has been also achieved by yttrium doping.<sup>24</sup> The occurrence of a heterostructured BiVO<sub>4</sub> formed by a tetragonal and monoclinic phase mixture has been demonstrated to have a clear beneficial effect on the final photoactivity of the system. Fan *et al.* reported that monoclinic/tetragonal heterostructured BiVO<sub>4</sub> in particular is expected to promote the separation of photo-induced electron–hole pairs.<sup>25</sup> These results clearly show that

Instituto de Ciencia de Materiales de Sevilla, Centro Mixto CSIC-Universidad de Sevilla, C/ Américo Vespucio, 49, 41092 Sevilla, Spain.  
E-mail: gcolon@icmse.csic.es; Tel: + 34 954489536

the behaviour of photoinduced charges is markedly dependent on the  $\text{BiVO}_4$  crystalline phases. Moreover, the presence of an interface in the monoclinic/tetragonal heterophase provides a spatial condition for charge transfer. This favours the separation of photoinduced electron-hole pairs, and changes the migration direction of the photoinduced carriers.

In the present paper, we describe the substantial improvements obtained by Er and Y co-doping for the  $\text{O}_2$  evolution reaction. The combination of these two lanthanide ions with specific influences over the structural and electronic features of the photocatalyst clearly affects its final photocatalytic activity. The correlation between different structural and electronic techniques with the photoactivity under different irradiation conditions would provide a possible explanation of the role of this co-doping.

## 2. Experimental

### 2.1 Sample preparation

The  $\text{BiVO}_4$  samples were prepared by a surfactant free hydrothermal method. First, 5 mmol of  $\text{Bi}(\text{NO}_3)_3 \cdot 5\text{H}_2\text{O}$  (Sigma-Aldrich,  $\geq 98.0\%$ ) and a stoichiometric amount of  $\text{Er}(\text{NO}_3)_3$  (0.75 at%) were dissolved in 10 mL of glacial acetic acid at room temperature. A second aqueous solution was prepared by dissolving the corresponding stoichiometric amount of  $\text{NH}_4\text{VO}_3$  (Sigma-Aldrich,  $\geq 99.0\%$ ) or  $\text{Y}(\text{NO}_3)_3$  (3.0 at%) in 60 mL of hot distilled water. Afterwards, the ammonium metavanadate solution was added to the erbium-bismuth nitrate aqueous solution and the process was accompanied by vigorous stirring. The pH of the obtained suspension was adjusted to 9.0 by adding concentrated  $\text{NH}_4\text{OH}$  (13 mol  $\text{L}^{-1}$ ). The slurry was encased in a Teflon vessel and heated at 140 °C for 20 hours. The obtained precipitate was then cooled until it reached room temperature, filtered and repeatedly washed and dried overnight at 120 °C. Afterwards, thus obtained samples were submitted to a further calcination treatment at 300 °C for 2 h.

Tetragonal  $\text{BiVO}_4$  (t- $\text{BiVO}_4$ ) has been also prepared as reference material. In this case we followed a similar procedure as for the m- $\text{BiVO}_4$ , but using triethylamine as precipitating agent instead.

### 2.2 Materials characterization

BET surface area and porosity measurements were carried out by  $\text{N}_2$  adsorption at 77 K using a Micromeritics 2010 instrument.

The chemical composition of the samples was studied by ICP analysis using a Horiba Jobin Yvon, Ultima 2.

X-ray diffraction (XRD) patterns were obtained using a Siemens D-501 diffractometer with Ni filter and graphite monochromator. The X-ray source was Cu  $\text{K}\alpha$  radiation (0.15406 nm). Rietveld analyses were performed using XPert HighScore Plus software for selected samples. The diffraction patterns were recorded with a  $2\theta$  of 10° to 120° with a step of 0.017° and 400 s per step. Crystallite sizes were obtained from Rietveld refinement.

The UV diffuse reflectance spectra were measured using an UV-vis spectrophotometer equipped with an integrating sphere (JASCO V-570). The reference sample used was a  $\text{BaSO}_4$  coated standard pattern.

Micro-Raman measurements were performed using a LabRAM Jobin Yvon spectrometer equipped with a microscope. Laser radiation ( $\lambda = 532$  and 780 nm) was used as the excitation source at 5 mW. All measurements were recorded under the same conditions (4 s of integration time and 10 accumulations) using a 100× magnification objective and a 125 mm pinhole.

### 2.3 Photocatalytic tests

MB oxidation reactions were performed using a batch reactor (150 mL) with a 200 W Xenon lamp. The intensity of the incident light on the solution measured with a HD2302 photometer (Delta OHM) was 90  $\text{W m}^{-2}$  and 500  $\text{W m}^{-2}$  for UV and vis-NIR spectral ranges, respectively. For this scope, an LP 471 UVA sensor with a spectral response of 315–400 nm and an LP 471 RAD sensor (spectral response 400–1050 nm) were used. The vis-NIR runs were performed using a cut-off filter ( $\lambda > 420$  nm) which assured the complete withdrawal of UV incident photons. In the oxidation tests, an air flow was employed to produce a homogenous suspension of the photocatalyst in the solution. Before each experiment, the catalysts (1 g  $\text{L}^{-1}$ ) were settled in suspension with the reagent mixture for 15 min. The blank experiment was performed without a catalyst, and no dye degradation was observed after 2 hours. The evolution of the initial MB (*ca.* 10 ppm) concentration was followed through the evolution of the characteristic 664 nm band, using a centrifuged aliquot of *ca.* 2 mL of the suspension (microcentrifuge Minispin, Eppendorf). The pH of the suspension was unchanged during the photo-degradation tests (pH  $\sim$  6.5) for all  $\text{BiVO}_4$  samples. Reaction rates were calculated assuming first order kinetics.

The photocatalytic activity of the samples was also evaluated for the photocatalytic oxygen evolution reaction from water in an  $\text{AgNO}_3$  aqueous solution (0.02 M). The reaction media was continuously thermostated at 23°–25 °C to prevent any significant effect of temperature. The catalyst suspension (1 g  $\text{L}^{-1}$ ) was firstly degassed with a  $\text{N}_2$  stream (150 mL  $\text{min}^{-1}$ ) for 30 min. After that, the  $\text{N}_2$  flow was settled at 15 mL  $\text{min}^{-1}$  and stabilised for 15 min. This nitrogen flow was used to displace the oxygen produced from the photoreactor head-space towards the GC measuring system. Then, the lamp (200 W Hg-Xe lamp, Oriel Instruments) was switched on and the effluent gases were analysed to quantify  $\text{O}_2$  production by gas chromatography (Agilent 490 micro GC), using a thermal conductivity detector connected to Molsieve 5A and Poraplot Q columns.

## 3. Results and discussion

The XRD patterns shown in Fig. 1 depict the evolution of the crystalline phase upon the incorporation of different dopant ions. As can be observed, the original monoclinic structure

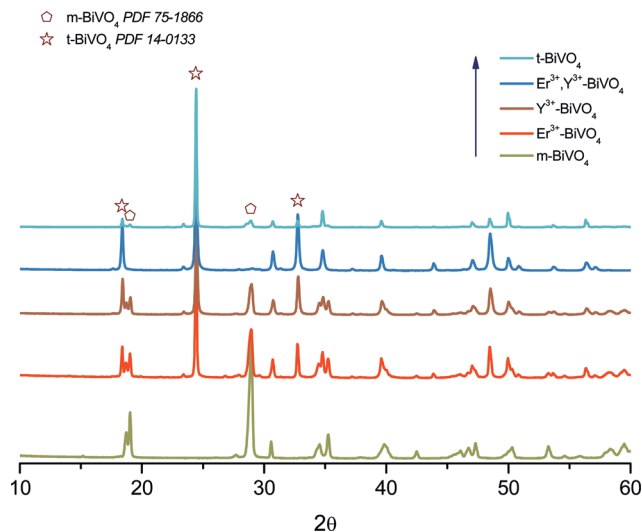


Fig. 1 XRD patterns for different  $\text{BiVO}_4$  catalysts obtained by hydrothermal synthesis at 140 °C for 20 h.

(PDF 75-1866) exhibited by bare  $\text{BiVO}_4$  is progressively lost as  $\text{Er}^{3+}$  and  $\text{Y}^{3+}$  are incorporated. The tetragonal phase (PDF 14-0133) stabilization is more pronounced when  $\text{Y}^{3+}$  is present. This marked stabilization is related to the higher doping level by yttrium in comparison to erbium. Finally, when both lanthanides are present only the tetragonal phase appears. For comparison we prepared a tetragonal reference sample, which exhibits a small fraction of the monoclinic phase.

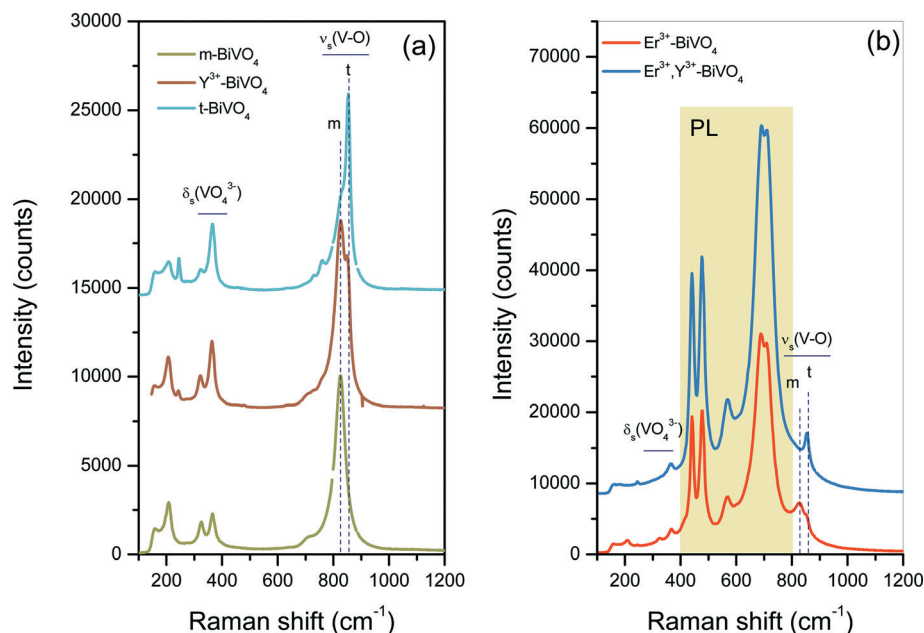
The structural features of the studied samples are summarized in Table 1. In the case of single doping, a clear tetragonal stabilization is observed. By observing the monoclinic and tetragonal cell volumes, it becomes apparent that the incorporation of the dopant appears quite different. Thus, while the monoclinic unit cell volume exhibits a slight increase as the lanthanides are incorporated, for the tetragonal phase a slight reduction in the cell volume is attained. This behavior would indicate a rather different location of the dopant in each  $\text{BiVO}_4$  structure. Thus, for the monoclinic structure  $\text{Ln}^{3+}$  would be placed in the interstitial sites. The calculated microstrain would evidence a more stressed structure, especially when yttrium is incorporated. On the other hand, the tetragonal structure would accommodate the dopant ions substitutionally in  $\text{Bi}^{3+}$  sites, tending to diminish the cell volume. This fact would be supported by considering the ionic radii of the dopants (89 pm and 104 pm for  $\text{Er}^{3+}$  and  $\text{Y}^{3+}$  respectively) with respect to  $\text{Bi}^{3+}$  (117 pm).<sup>26</sup> This cell

contraction would also provoke a structural stress, giving a higher microstrain in comparison with undoped t- $\text{BiVO}_4$ . In accordance with this behavior, the co-doped system also displays this effect. The pure tetragonal structure shows a significantly lower cell volume, which would indicate the substitutional occupation of the lanthanide ions.

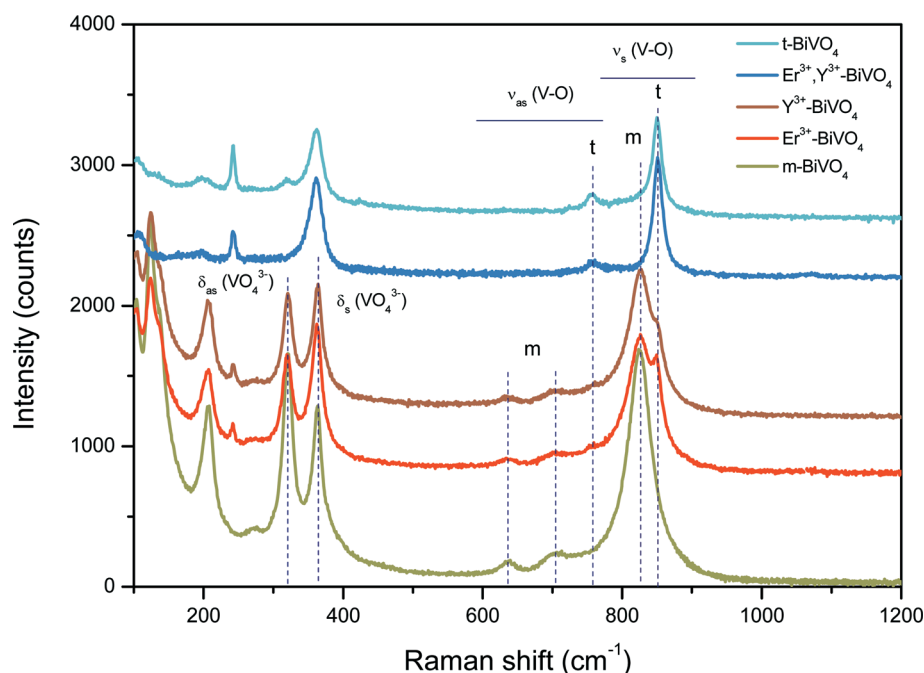
Raman spectroscopy is an effective tool for the structural characterization of materials. In Fig. 2 we show the Raman spectra for the studied samples registered upon green laser excitation. The monoclinic  $\text{BiVO}_4$  Raman spectrum is characterized by the presence of typical bands at 210, 324, 366, 640, 710 and 825  $\text{cm}^{-1}$ .<sup>27</sup> These two latter bands are associated with stretching modes corresponding to the V–O bond, and provide valuable structural information.<sup>28</sup> For lanthanide doped samples, the monoclinic-to-tetragonal transition by the  $\nu_s$  (V–O) band shift from 820  $\text{cm}^{-1}$  to 850  $\text{cm}^{-1}$ , and the disappearance of the  $\delta$  ( $\text{VO}_4^{3-}$ ) doublet of the monoclinic phase, can be seen (Fig. 2a). As has previously been reported, Raman spectra containing rare earth ions are strongly affected by the luminescence emission. Thus,  $\text{Er}^{3+}$ -containing samples exhibit noticeable luminescence emission bands (Fig. 2b). It is worth noting that these luminescence bands appear highly intense for the co-doped  $\text{BiVO}_4$  compared with  $\text{Er}^{3+}$ - $\text{BiVO}_4$ . This would indicate that the presence of yttrium improves upon the luminescent properties of erbium to a certain extent. This fact has been previously reported for  $\text{Er}^{3+}$ - $\text{Y}^{3+}$  co-doped  $\text{TiO}_2$ .<sup>29</sup> Thus, Ting *et al.* argued that the distorted local structure of the  $\text{Er}^{3+}$  ions due to the presence of the yttrium could increase the probability of a normally forbidden intra-4f transition, improving the photoluminescence process. In order to examine the structural evolution of the  $\text{BiVO}_4$  samples without the interference of erbium luminescence emission, we performed Raman spectroscopy by red laser excitation (Fig. 3). From these spectra, the monoclinic-to-tetragonal transition due to lanthanide doping can be clearly seen. Thus the  $\nu_s$  (V–O) stretching mode at 825  $\text{cm}^{-1}$  for the monoclinic structure appears with a shoulder at a higher Raman shift when erbium or yttrium is incorporated. This evidently denotes the co-existence of both phases, as was suggested by the XRD results. Moreover, the co-doped  $\text{BiVO}_4$  clearly shows a single band at 850  $\text{cm}^{-1}$  denoting the exclusive presence of a tetragonal phase. From the Raman shift position corresponding to the symmetric stretching mode, it is possible to attain information about the V–O bond length in the  $\text{VO}_4^{3-}$  tetrahedron through the following expression:<sup>30</sup>

Table 1 Structural characterization of the  $\text{BiVO}_4$  and  $\text{Er}^{3+}$ ,  $\text{Y}^{3+}$  doped catalysts

Samples	Monoclinic			Tetragonal		Microstrain		Monoclinic cell volume ( $\text{\AA}^3$ )	Tetragonal cell volume ( $\text{\AA}^3$ )	Tetragonal %
	a	b	c	a = b	c	Monoclinic	Tetragonal			
m- $\text{BiVO}_4$	5.2015	5.1008	11.7198	—	—	0.005	—	310.95	—	0
t- $\text{BiVO}_4$	—	—	—	7.3047	6.4613	—	0.040	—	344.6	95
$\text{Er}^{3+}$ - $\text{BiVO}_4$	5.2220	5.1031	11.7080	7.2969	6.4533	0.049	0.068	312.00	344.6	55
$\text{Y}^{3+}$ - $\text{BiVO}_4$	5.2062	5.1007	11.7200	7.2976	6.4540	0.206	0.145	311.23	343.9	68
$\text{Er}^{3+}$ , $\text{Y}^{3+}$ - $\text{BiVO}_4$	—	—	—	7.2955	6.4535	—	0.153	—	343.8	100



**Fig. 2** Raman spectra obtained upon green laser (532 nm) excitation for: a) undoped m- and t-BiVO<sub>4</sub> and Y<sup>3+</sup>-BiVO<sub>4</sub> systems; b) Er<sup>3+</sup>-BiVO<sub>4</sub> and Er<sup>3+</sup>, Y<sup>3+</sup>-BiVO<sub>4</sub> systems (PL denotes the photoluminescence bands corresponding to the presence of Er<sup>3+</sup>).



**Fig. 3** Raman spectra for different BiVO<sub>4</sub> catalysts obtained upon red laser (780 nm) excitation.

$$\nu(\text{cm}^{-1}) = 21349e^{(-1.9176R(\text{\AA}))}$$

In Table 2 we present the calculated V-O bond distances ( $R$ ) for bare BiVO<sub>4</sub> and the doped systems. By observing the calculated bond lengths it is worth noting that while the incorporation of erbium does not induce a significant distortion in the VO<sub>4</sub><sup>3-</sup> tetrahedron in either the monoclinic or tetragonal structure, yttrium doping induces a slight decrease

in both structures.<sup>31</sup> This result is in accordance to the microstrain values for Er<sup>3+</sup>-BiVO<sub>4</sub> shown in Table 1, and could be correlated to the lower ionic radius of Er<sup>3+</sup> compared to Y<sup>3+</sup>, as well as to the lower erbium doping level. The shorter bond length in yttrium doped systems would indicate a stronger packed tetragonal structure and would affect the lone pair distortion around the bismuth cation.<sup>27</sup> It has been argued that structural distortion is directly proportional to the hole mobility.<sup>32</sup>



**Table 2** Structural features found by Raman characterization for BiVO<sub>4</sub> and Er<sup>3+</sup>, Y<sup>3+</sup> doped catalysts<sup>a</sup>

Samples	Raman frequency (cm <sup>-1</sup> )		Bond length V–O (Å)	
	Monoclinic	Tetragonal	Monoclinic	Tetragonal
m-BiVO <sub>4</sub>	824.99	—	1.6966	—
t-BiVO <sub>4</sub>	—	850.15	—	1.6809
Er <sup>3+</sup> -BiVO <sub>4</sub>	825.13	850.02	1.6965	1.6810
Y <sup>3+</sup> -BiVO <sub>4</sub>	825.88	851.63	1.6960	1.6800
Er <sup>3+</sup> ,Y <sup>3+</sup> -BiVO <sub>4</sub>	—	—	—	1.6803

<sup>a</sup> The positions of the most intense bands near 825 cm<sup>-1</sup> and 850 cm<sup>-1</sup> were determined by fitting to the Lorentzian peak function.

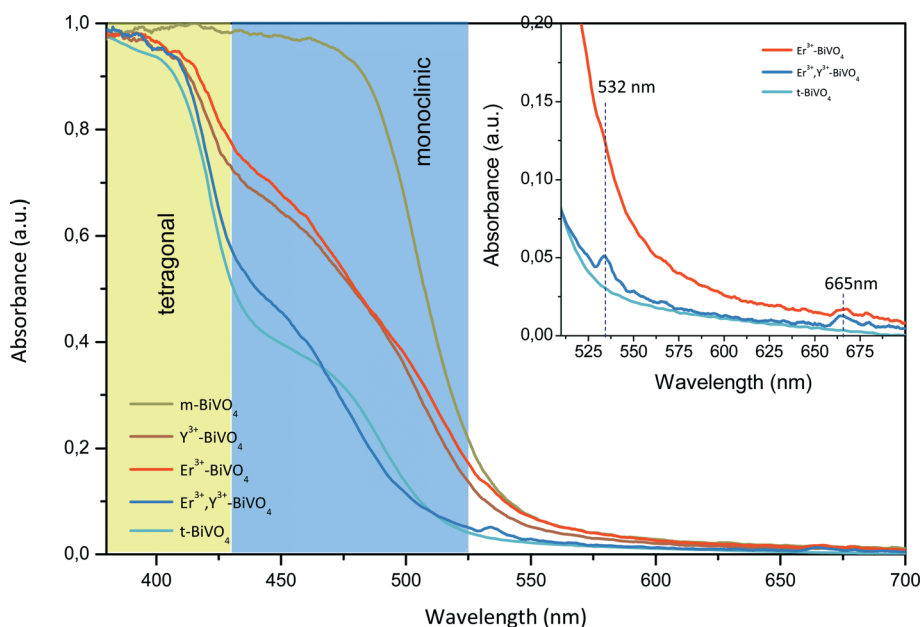
In order to study the electronic states of the different systems studied, UV-vis DRS spectra were taken (Fig. 4). As can be seen from the figure, the absorption edges of the doped BiVO<sub>4</sub> samples varied in an order which matched the structural changes discussed above. It can be noticed that t-BiVO<sub>4</sub> shows a small absorption in the visible range. This small contribution denotes the presence of a residual m-BiVO<sub>4</sub> that was previously detected from the XRD results (see Table 1). Even the Er<sup>3+</sup>,Y<sup>3+</sup>-BiVO<sub>4</sub> sample presents a small shoulder in this region, in spite of Rietveld analysis and the Raman spectrum confirming that the monoclinic fraction present was negligible. Accordingly, the different phase compositions of BiVO<sub>4</sub> result in different band gaps (Table 3). As the monoclinic-to-tetragonal transition is taking place, the band gaps tend to shift from the visible region to the UV light region.

Other physicochemical properties such as the chemical composition and surface area of the studied systems are summarized in Table 3. The effectiveness of the doping is supported by chemical analysis using the ICP technique. The

relative contents of erbium and yttrium with respect to bismuth are in accordance with the nominal values. Regarding the surface area values, it can be observed that the structural changes are clearly accompanied by a certain modification in the surface area values. As has been widely reported, tetragonal phase BiVO<sub>4</sub> exhibits relatively larger surface area values compared to the monoclinic phase.<sup>23,24</sup>

The morphology of BiVO<sub>4</sub> has been extensively reported to be dependent on the preparation route.<sup>33</sup> In our case, bare m-BiVO<sub>4</sub> shows a rod-like morphology (Fig. 5a) while t-BiVO<sub>4</sub> is composed of square-bar particles (Fig. 5b). As the erbium or yttrium ion is incorporated, the morphology of the sample clearly denotes the mixture of the two phases present (Fig. 5c and d).<sup>33</sup> For erbium doping the tetragonal particles present a clear evolution from a square-bar shape toward a thinner acicular morphology. Meanwhile, the monoclinic sample seems to evolve towards a well-defined prism-like morphology. As can be seen, the incorporation of yttrium induces quite a drastic change in morphology. The tetragonal acicular particles seem to decrease in size, showing a rod-like morphology.<sup>24</sup> Co-doped BiVO<sub>4</sub> follows the above mentioned evolution and only small rice-like particles appear (200–500 nm length and 100 nm width) (Fig. 5e and f).

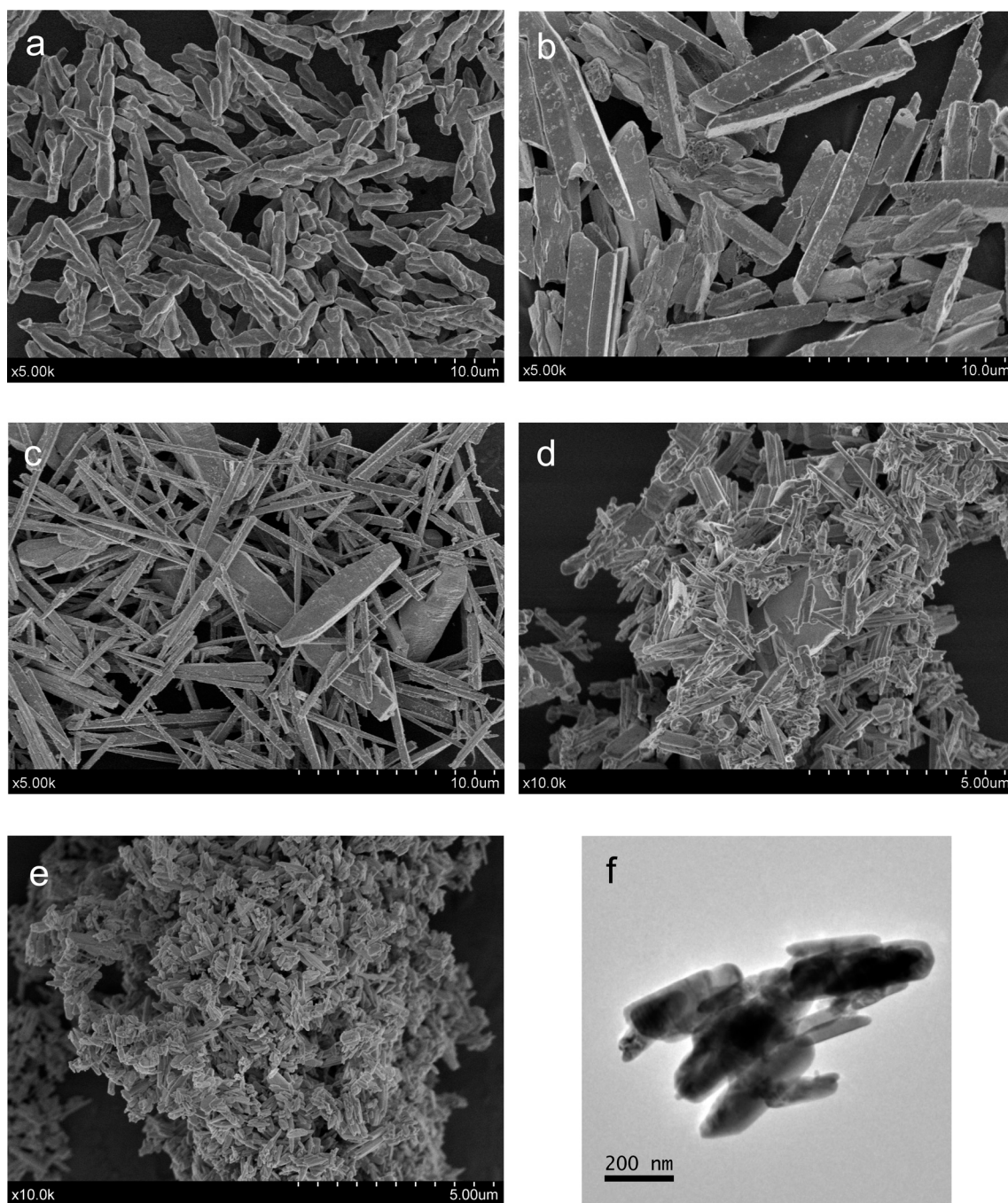
In Fig. 6 we show the photocatalytic activity of the studied systems. The incorporation of either an erbium or yttrium ion into the BiVO<sub>4</sub> structure produces a clear improvement in the photodegradation of MB, with Er<sup>3+</sup>-BiVO<sub>4</sub> being slightly more active than Y<sup>3+</sup>-BiVO<sub>4</sub> (Fig. 6a). In both cases, the main crystalline phase was tetragonal, although for Er<sup>3+</sup>-BiVO<sub>4</sub> the monoclinic fraction is slightly higher. The simultaneous Er<sup>3+</sup> and Y<sup>3+</sup> doping improves the photocatalytic activity compared to single doped systems, despite the fact that a pure tetragonal phase is present. If we compare the calculated reaction



**Fig. 4** Evolution of diffuse reflectance spectra for different bare and doped BiVO<sub>4</sub> catalysts obtained by hydrothermal synthesis at 140 °C for 20 h (inset: comparison of t-BiVO<sub>4</sub> and Er-doped systems).

**Table 3** Surface, electronic and photocatalytic characterization for the BiVO<sub>4</sub> and Er<sup>3+</sup>,Y<sup>3+</sup> doped catalysts

Samples	BET (m <sup>2</sup> g <sup>-1</sup> )	Band gap (eV)		Ln <sup>3+</sup> content		MB degradation reaction rate (10 <sup>-4</sup> s <sup>-1</sup> )		O <sub>2</sub> evolution (μmol h <sup>-1</sup> g <sup>-1</sup> )
		Monoclinic	Tetragonal	Er <sup>3+</sup> /Bi <sup>3+</sup>	Y <sup>3+</sup> /Bi <sup>3+</sup>	UV-vis-NIR	vis-NIR	
m-BiVO <sub>4</sub>	<1	2.39	—	—	—	1.26	0.458	53
t-BiVO <sub>4</sub>	5	—	2.86	—	—	0.99	0.061	37
Er <sup>3+</sup> -BiVO <sub>4</sub>	2	2.39	2.75	0.006	—	5.10	0.149	320
Y <sup>3+</sup> -BiVO <sub>4</sub>	3	2.38	2.77	—	0.033	4.03	0.141	285
Er <sup>3+</sup> ,Y <sup>3+</sup> -BiVO <sub>4</sub>	5	—	2.83	0.006	0.029	6.55	0.205	425

**Fig. 5** FESEM images of the different BiVO<sub>4</sub> systems: a) bare m-BiVO<sub>4</sub>; b) bare t-BiVO<sub>4</sub>; c) Er<sup>3+</sup>-BiVO<sub>4</sub>; d) Y<sup>3+</sup>-BiVO<sub>4</sub>; e) Er<sup>3+</sup>,Y<sup>3+</sup> co-doped BiVO<sub>4</sub>; f) a TEM image of the Er<sup>3+</sup> and Y<sup>3+</sup> co-doped BiVO<sub>4</sub>.

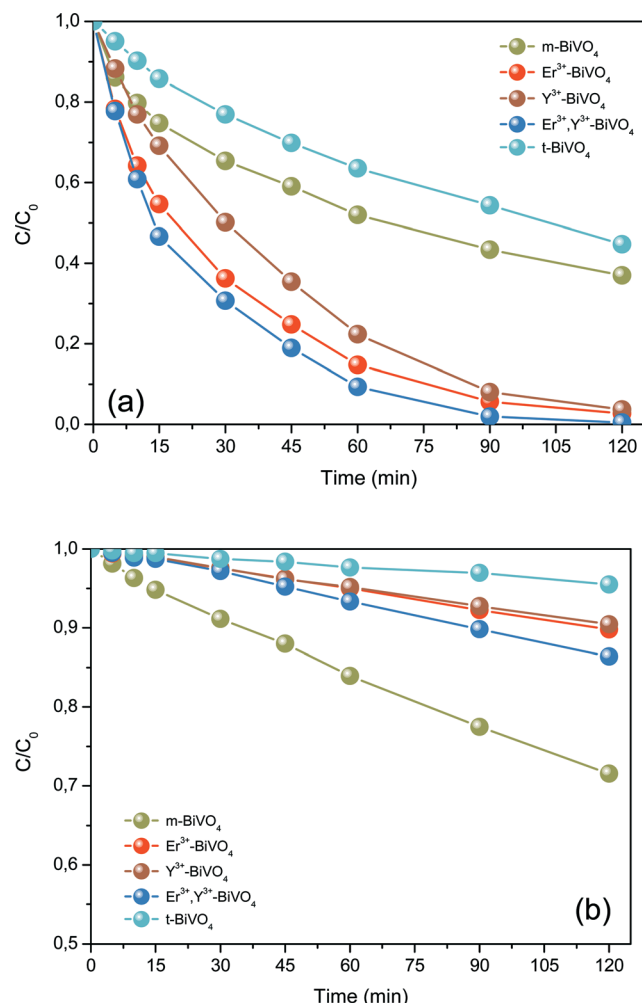


Fig. 6 Evolution of MB concentration with photodegradation time for different  $\text{BiVO}_4$  catalysts. a) Upon UV-vis-NIR irradiation; b) upon vis-NIR irradiation.

rates of this later sample with the corresponding rates for  $\text{m-BiVO}_4$  and  $\text{t-BiVO}_4$ , a dramatic enhancement is displayed (Table 3). For the  $\text{Er}^{3+}$  and  $\text{Y}^{3+}$  co-doped sample the surface area value is slightly higher than for  $\text{m-BiVO}_4$ . However, a comparison with  $\text{t-BiVO}_4$  clearly shows that the controlling parameter in the photoactivity is something other than the BET surface area.

In order to elucidate the specific role of erbium on the reaction mechanism, we performed the degradation reaction under vis-NIR irradiation (Fig. 6b). As expected,  $\text{m-BiVO}_4$  shows the best photocatalytic performance while  $\text{t-BiVO}_4$  shows a negligible photoactivity. However, although all doped systems show a tetragonal-rich structure, their photoactivity under vis-NIR irradiation appears somewhat improved (Table 3). From this result it is clear that – besides the increase of surface area values due to the presence of a tetragonal phase in single doped  $\text{BiVO}_4$  compared to  $\text{m-BiVO}_4$  – the particular structural features of the systems (*i.e.* the monoclinic-tetragonal heterostructure) might be in principle the reason behind the photocatalytic activity enhancement. In this sense, as

reported by Fan *et al.*, the monoclinic-tetragonal heterostructured  $\text{BiVO}_4$  in particular is expected to promote the separation of photoinduced electron-hole pairs.<sup>25</sup> These authors proposed that enhanced photoactivity would be achieved by the optimization of the electron-hole separation due to the heterostructure formation. On this basis, we could state that the conjunction of morphological and structural features clearly provides a better photocatalytic performance. Moreover, the presence of erbium would also particularly affect the photoelectronic mechanism under vis-NIR excitation, which could explain the better performance of  $\text{Er}^{3+}\text{-BiVO}_4$  compared to  $\text{Y}^{3+}\text{-BiVO}_4$ .<sup>23</sup> As we have previously reported, a cooperative luminescence effect is observed for Er-doped  $\text{t-BiVO}_4$ , which would explain its vis-NIR photoactivity. In the case of co-doped  $\text{BiVO}_4$ , which exhibits a pure tetragonal structure, the photocatalytic enhancement cannot be associated with the presence of a phase heterostructure. Furthermore, the reaction rate for this system is notably higher than for the single doped systems. Lower photoactivity reported for  $\text{t-BiVO}_4$  in the literature was explained by considering the wider band gap for this phase. Thus, in our case the increased photoluminescence observed in the Raman spectrum for  $\text{Er}^{3+}, \text{Y}^{3+}\text{-BiVO}_4$  compared to that for  $\text{Er}^{3+}\text{-BiVO}_4$  upon illumination with 532 nm laser would suggest the participation of such a luminescence process in the overall mechanism. In summary, the notably enhanced photoactivity observed upon sun-like irradiation would be associated with a double cooperative mechanism. On one hand, yttrium incorporation would affect the conduction band position.<sup>31</sup> The participation of the Y 4d orbital in the conduction band hybridization would shift it to a higher position compared to the conduction band for  $\text{m-BiVO}_4$ . Thus,  $\text{Y}^{3+}$  would help to improve the photon efficiency, enhancing the UV-photoassisted process by increasing the electron-hole separation driving force. Secondly, the presence of erbium and the associated luminescence up-conversion process could improve the photoefficiency within the vis-NIR region by increasing the number of absorbed photons. A similar effect has already been observed for  $\text{Er}^{3+}$  doped  $\text{TiO}_2$ , for which an up-conversion mechanism would be responsible in part for its better photocatalytic behaviour under vis-NIR irradiation.<sup>22,34</sup>

The durability of the  $\text{Er,Y-BiVO}_4$  system was evaluated through recycling the used catalyst (Fig. 7). For each cycle, the catalyst was collected by filtration and washed. As can be observed from consecutive degradation cycles, there was no apparent loss of photocatalytic activity across the four cycles performed. The diminution of photocatalytic activity was less than 2%. Therefore, it can be deduced that the  $\text{Er,Y}$  co-doped  $\text{BiVO}_4$  has good photostability and reusability which indicates its potential for industrial utilization.

Furthermore, Fig. 8 shows the photocatalytic water oxidation activity of different  $\text{BiVO}_4$  samples, from an aqueous solution containing  $\text{AgNO}_3$  as a sacrificial reagent under sunlight irradiation. Despite the fact that our  $\text{m-BiVO}_4$  does not initially show an excellent photocatalytic performance such



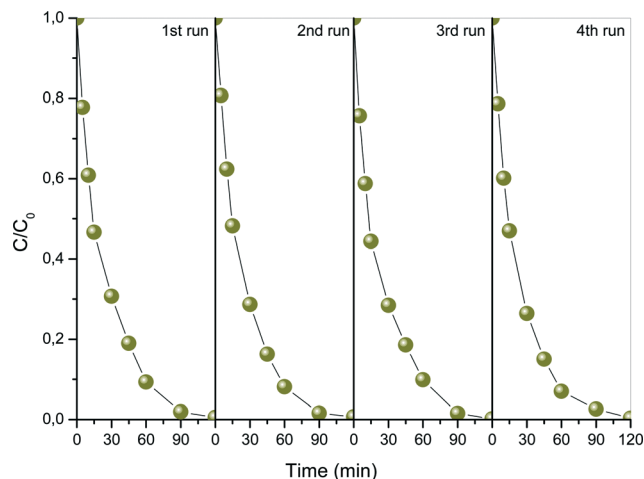


Fig. 7 Reusability properties of the  $\text{Er}^{3+}, \text{Y}^{3+}$ - $\text{BiVO}_4$  system for the MB degradation reaction.

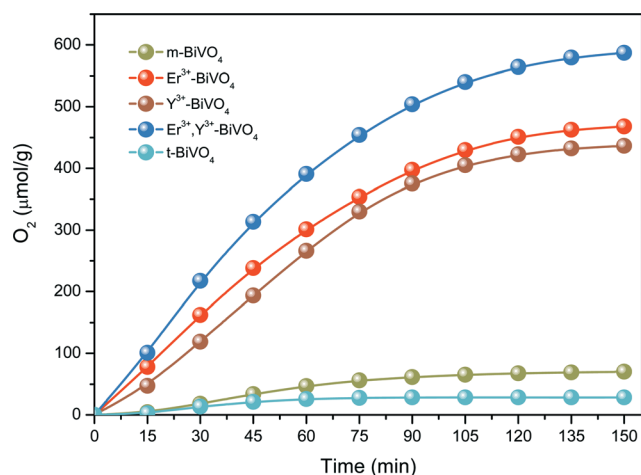


Fig. 8 Photocatalytic  $\text{O}_2$  evolution for different  $\text{BiVO}_4$  samples from aqueous  $\text{AgNO}_3$  solutions ( $0.02 \text{ mol L}^{-1}$ ) as a function of the irradiation time.

as that reported in ref. 10,  $\text{O}_2$  evolution of our m- $\text{BiVO}_4$  is in the range of other reported bismuth vanadates.<sup>35,36</sup> Moreover, the  $\text{O}_2$  evolution for different doped  $\text{BiVO}_4$  catalysts plainly denotes a notably beneficial effect. In all cases, the  $\text{O}_2$  evolution rates for these samples are markedly improved with respect to bare m- or t- $\text{BiVO}_4$  (Table 3). This trend is in accordance with the previous behaviour for the MB photodegradation reaction, as discussed above. Moreover, the photocatalytic performance shown by the  $\text{Er}^{3+}, \text{Y}^{3+}$  co-doped  $\text{BiVO}_4$  appears significantly enhanced compared to the single doped systems ( $425 \mu\text{mol h}^{-1} \text{ g}^{-1}$  vs. ca.  $300 \mu\text{mol h}^{-1} \text{ g}^{-1}$ ). Thus, the calculated reaction rate for the co-doped system is 8 times higher than that for the m- $\text{BiVO}_4$  as reported in the present work. By observing the reaction rate for t- $\text{BiVO}_4$ , this enhancement cannot be exclusively associated with the increase in surface area or a higher UV adsorption. The occurrence of both lanthanide ion dopants leads to a synergistic effect that could be explained by considering their different roles.

## 4. Conclusions

We have obtained a highly active  $\text{Er}^{3+}, \text{Y}^{3+}$ - $\text{BiVO}_4$  system which exhibits a tetragonal structure. Hydrothermal synthesis leads to homogeneous  $\text{BiVO}_4$  rice-like nanoparticles ca. 200–400 nm in length. Chemical and structural analysis confirms the incorporation of lanthanide dopant ions into the  $\text{BiVO}_4$  structure. The photocatalytic activity for methylene blue degradation and for  $\text{O}_2$  evolution clearly evidences the beneficial effect of doping. Moreover, it is worth noting that the tetragonal phase co-doped  $\text{BiVO}_4$  shows a significantly higher photoactivity than bare m- $\text{BiVO}_4$  and t- $\text{BiVO}_4$ . From the photocatalytic experiments we tentatively propose a double mechanism which could explain the improved photoactivity of the doped systems. On one hand, the presence of  $\text{Er}^{3+}$  and  $\text{Y}^{3+}$  improved the electronic charge separation process, enhancing the UV-photoassisted process. This mechanism is consistent with a classical doping conception, since we used  $\text{BiVO}_4$  as the host material. Moreover, it can be seen that there is a small contribution of vis-NIR photons to the UV-active tetragonal co-doped  $\text{BiVO}_4$  in the overall mechanism, probably due to an energy transfer process from the erbium ions. As a result, the  $\text{Er}^{3+}, \text{Y}^{3+}$  co-doped  $\text{BiVO}_4$  shows a notably improved photoactivity compared to the m- $\text{BiVO}_4$ . By adjusting the band and photon absorption features, we propose a highly active material for  $\text{O}_2$  evolution from a water splitting reaction.

## Acknowledgements

Financial support from projects P09-FQM-4570 and ENE2011-24412 is fully acknowledged. S. Obregón Alfaro thanks CSIC for the concession of a JAE-Pre grant.

## References

- 1 D. Ravelli, D. Dondi, M. Fagnoni and A. Albini, *Chem. Soc. Rev.*, 2009, 38, 1999–2011.
- 2 M. Pelaez, N. T. Nolan, S. C. Pillai, M. K. Seery, P. Falaras, A. G. Kontos, P. S. M. Dunlop, J. M. J. Hamilton, J. A. Byrne, K. O'Shea, M. H. Entezari and D. D. Dionysiou, *Appl. Catal., B*, 2012, 125, 331–349.
- 3 M. Maeda and K. Domen, *J. Phys. Chem. C*, 2007, 111, 7851–7861.
- 4 A. Kubacka, M. Fernández-García and G. Colón, *Chem. Rev.*, 2012, 112, 1555–1614.
- 5 A. Kudo and Y. Miseki, *Chem. Soc. Rev.*, 2009, 38, 253–278.
- 6 K. Maeda, *J. Photochem. Photobiol., C*, 2011, 12, 237–268.
- 7 K. Sayama, R. Yoshida, H. Kusama, K. Okabe, Y. Abe and H. Arakawa, *Chem. Phys. Lett.*, 1997, 277, 387–391.
- 8 K. Maeda, *ACS Catal.*, 2013, 3, 1486–1503.
- 9 J. Yang, D. Wang, X. Zhou and C. Li, *Chem.-Eur. J.*, 2013, 19, 1320–1326.
- 10 A. Kudo, K. Omori and H. Kato, *J. Am. Chem. Soc.*, 1999, 121, 11459–11467.



- 11 Y. Park, K. J. McDonald and K. S. Choi, *Chem. Soc. Rev.*, 2013, **42**, 2321–2337.
- 12 D. Ke, T. Peng, L. Ma, P. Cai and K. Dai, *Inorg. Chem.*, 2009, **48**, 4685–4691.
- 13 H. Jiang, H. Dai, X. Meng, L. Zhang, J. Deng, Y. Liu and C. T. Au, *J. Environ. Sci.*, 2012, **24**, 449–457.
- 14 L. Pan, X. Liu, Z. Sun and C. Q. Sun, *J. Mater. Chem. A*, 2013, **1**, 8299–8326.
- 15 S. Tokunaga, H. Kato and A. Kudo, *Chem. Mater.*, 2001, **13**, 4624–4628.
- 16 H. M. Zhang, J. B. Liu, H. Wang, W. X. Zhang and H. Yan, *J. Nanopart. Res.*, 2008, **10**, 767–774.
- 17 Y. K. Kho, W. Y. Teoh, A. Iwase, L. Mädler, A. Kudo and R. Amal, *ACS Appl. Mater. Interfaces*, 2011, **3**, 1997–2004.
- 18 Z. Zhang, W. Wang, J. Xu, M. Shang, J. Ren and S. Sun, *Catal. Commun.*, 2011, **13**, 31–34.
- 19 T. Zhou, J. Hu and J. Li, *Appl. Catal., B*, 2011, **110**, 221–230.
- 20 Z. X. Li, F. B. Shi, T. Zhang, H. S. Wu, L. D. Sun and C. H. Yan, *Chem. Commun.*, 2011, **47**, 8109–8111.
- 21 R. Adhikari, G. Gyawali, S. H. Cho, R. Narro-García, T. Sekino and S. W. Lee, *J. Solid State Chem.*, 2014, **209**, 74–81.
- 22 S. Obregón and G. Colón, *Chem. Commun.*, 2012, **48**, 7865–7867.
- 23 S. Obregón, S. W. Lee and G. Colón, *Dalton Trans.*, 2014, **43**, 311.
- 24 S. Usai, S. Obregón, A. I. Becerro and G. Colón, *J. Phys. Chem. C*, 2013, **117**, 24479–24484.
- 25 H. Fan, T. Jiang, H. Li, D. Wang, L. Wang, J. Zhai, D. He, P. Wang and T. Xie, *J. Phys. Chem. C*, 2012, **116**, 2425–2430.
- 26 R. D. Shannon, *Acta Crystallogr., Sect. A: Cryst. Phys., Diffraction, Theor. Gen. Crystallogr.*, 1976, **32**, 751–767.
- 27 S. R. M. Thalluri, C. Martínez-Suarez, A. Virga, N. Russo and G. Saracco, *Int. J. Chem. Eng. Appl.*, 2013, **4**, 305–309.
- 28 J. Yu and A. Kudo, *Chem. Lett.*, 2005, **34**, 850–851.
- 29 C. C. Ting, S. Y. Chen, W. F. Hsieh and H. Y. Lee, *J. Appl. Phys.*, 2001, **90**, 5564–5569.
- 30 F. D. Hardcastle and I. E. Wachs, *J. Phys. Chem.*, 1991, **95**, 5031–5041.
- 31 H. Liu, J. Yuan, Z. Jiang, W. Shangguan, H. Einaga and Y. Teraoka, *J. Mater. Chem.*, 2011, **21**, 16535–16543.
- 32 J. Yu and A. Kudo, *Adv. Funct. Mater.*, 2006, **16**, 2163–2169.
- 33 S. Obregón, A. Caballero and G. Colón, *Appl. Catal., B*, 2012, **117–118**, 59–66.
- 34 S. Obregón, A. Kubacka, M. Fernández-García and G. Colón, *J. Catal.*, 2013, **299**, 298–306.
- 35 W. Yao and J. Ye, *Chem. Phys. Lett.*, 2008, **450**, 370–374.
- 36 J. Yu, Y. Zhang and A. Kudo, *J. Solid State Chem.*, 2009, **182**, 223–228.